Squeezing Out Nanoparticles from Perovskites: Controlling Exsolution with Pressure

Andrés López-García, Sonia Remiro-Buenamañana, Dragos Neagu, Alfonso J. Carrillo,* and José Manuel Serra*

Nanoparticle exsolution has emerged as a versatile method to functionalize oxides with robust metallic nanoparticles for catalytic and energy applications. By modifying certain external parameters during thermal reduction (temperature, time, reducing gas), some morphological and/or compositional properties of the exsolved nanoparticles can be tuned. Here, it is shown how the application of high pressure (<100 bar H_2) enables the control of the exsolution of ternary FeCoNi alloyed nanoparticles from a double perovskite. H_2 pressure affects the lattice expansion and the nanoparticle characteristics (size, population, and composition). The composition of the alloyed nanoparticles could be controlled, showing a reversal of the expected thermodynamic trend at 10 and 50 bar, where Fe becomes the main component instead of Ni. In addition, pressure drastically lowers the exsolution temperature to 300 °C, resulting in unprecedented highly-dispersed and small-sized nanoparticles with a similar composition to those obtained at 600 °C and 10 bar. The mechanisms behind the effects of pressure on exsolution are discussed, involving kinetic, surface thermodynamics, and lattice-strain factors. A volcano-like trend of the exsolution extent suggests that competing pressure-dependent mechanisms govern the process. Pressure emerges as a new design tool for metallic nanoparticle exsolution enabling novel nanocatalysts and surface-functionalized materials.

1. Introduction

In the past decade, exsolution has gained interest in functionalizing the surface of mixed-oxide materials, i.e., perovskites, with nanoparticles (NPs) over other classic deposition methods, such as impregnation.[1] Exsolution is based on the migration of metal cations across the oxide bulk to form NPs on the oxide surface. This usually happens under reducing conditions (generally, H_2 flow), medium-high temperatures (500–1000 °C), and prolonged treatment times, typically conducing to the formation of reduced NPs, e.g., in the metallic state. Metal cations migrate from the structure of the material itself into its surface, where they nucleate, grow, and, finally, constitute NPs that remain anchored, partially embedded in the surface ("socketed").[2] This fact brings several advantages over other functionalizing methods, i.e., increased resistance to high-temperature sintering or coke formation,[3] better control over the size and distribution of the NPs, and the possibility of reversible exsolution.[4–8] In addition, morphological characteristics of the exsolved NPs can be modified, typically through changes in the external parameters of the thermal reduction treatment. Currently, the effect of changes in temperature, time, and even gas flow on the exsolution process has been previously studied.[9–11] By adjusting these parameters, i.e., temperature and time, exsolved NPs attributes can be tuned, like their dispersion,[12] size, or shape[13] (**Figure 1**).

Despite its many advantages, the exsolution process is still susceptible to being improved and, thereby, reaching higher versatility and efficiency as a surface-functionalization process. Efforts are underway to reduce exsolution requirements by lowering treatment temperature and times and avoiding using H_2 as a reducing agent. In this context, two ways are the most likely to achieve this goal: i) an optimization in the design of the materials favored to exsolve at lower temperatures and ii) an exploration of alternative methods to trigger exsolution without needing the classical reducing conditions. Related to the design strategy, A-site deficiency has been proved to trigger exsolution[14,15] and thus increase the number of exsolved NPs. Guo et al. proved bimetallic Ni-Ru exsolution between 350 and 450 °C with an A-site deficient double perovskite, $La_{2-x}NiRuO_{6-\delta}$, using 5% H_2/Ar flow.[16] This exsolution at 350 °C is among the lowest exsolving temperatures described using H_2 flow as a reducing agent, together with Chen et al. (300 °C, Ag NPs exsolution from $AgNbO_3$).[17] A

A. López-García, S. Remiro-Buenamañana, A. J. Carrillo, J. M. Serra
Instituto de Tecnología Química (Universitat Politècnica de
València-Consejo Superior de Investigaciones Científicas)
València 46022, Spain
E-mail: alcardel@itq.upv.es; jmserra@itq.upv.es
D. Neagu
Department of Chemical and Process Engineering
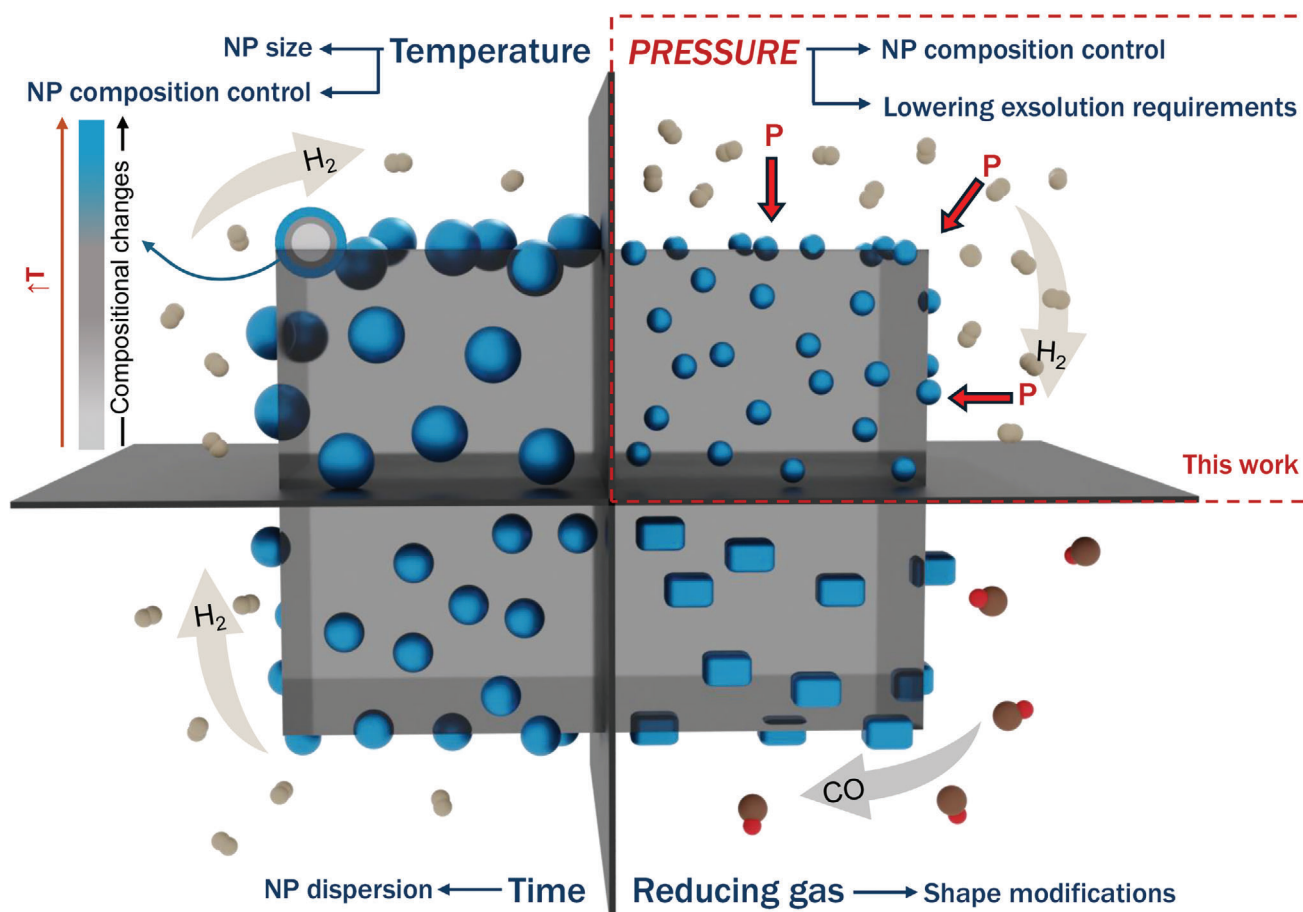University of Strathclyde
Glasgow G1 1XQ, United Kingdom

External treatment parameters modification: controlling exsolution properties

Figure 1. Schematic representation of the different treatment parameters that can be used to modify morphological and/or compositional properties of the exsolved NPs. The increasing temperature usually tailors NP growth, but also compositional changes when involving alloyed exsolution. Longer exposure times to thermal reduction treatment mainly lead to higher NP populations, whereas alternative reducing atmosphere to H₂ can trigger NP shape modifications. In this work, the effect of pressure during the exsolution process is evaluated, and a remarkable impact on alloyed NPs composition is observed, together with the possibility of lowering exsolution treatment requirements.

proper design strategy can also be based on a point-defect introduction, leading to an enhanced exsolution process via oxygen-vacancy engineering.[18] On the other hand, alternative exsolution methods avoiding using chemical reducing agents have been described. Electrochemical reduction[19] showed great exsolution results for $La_{0.43}Ca_{0.37}Ni_{0.06}Ti_{0.94}O_{3-\gamma}$ with no H_2 involved and requiring significantly less time (150 s) compared to thermal exsolution (usually, several hours). Nevertheless, this method needed high temperatures to be effective, and the material had to be fabricated as an electrode in a solid-oxide electrochemical cell. In addition, plasma-driven[20] exsolution proved to be an alternative path to reduce this same perovskite, also exhibiting good exsolution results with shorter times (1 h) and significantly lower temperatures[21] than thermal reduction. More recently, microwave-driven processes proved the exsolution of Ni NPs from A-site deficient perovskites, with no additional heating or need of reducing gases, involving remarkably shorter treatments (1-min pulses) than thermal exsolution.[22] Last, metallic NP exsolution has also been triggered with ion irradiation, which allowed the control of morphological properties besides

the composition of the Fe-Ni exsolved alloys.[23] These methods illustrate alternative exsolution methods circumventing the usual constraints of thermal reduction.

Despite the promise of new mechanisms to drive exsolution on mixed-oxide materials, thermal reduction keeps a prominent place as a way to functionalize materials with in-situ grown NPs. Besides the modification of exsolved NPs attributes with a treatment parameters adjustment, more efficient thermal exsolution could also be achieved through a condition-adjustment strategy. Among all the possible tunable external treatment parameters, to the best of our knowledge, the effect of pressure as part of the external treatment modification strategy has not been evaluated until now.[24] If used as a driving force for exsolution, pressure could align notably well with specific application processes, e.g., those operated at high H_2 pressure, such as CO_2 hydrogenation or ammonia synthesis,[25,26] to boost catalyst activity and stability. High-pressure exsolution can be a valuable tool for catalytic H_2 production or utilization processes. In particular, the use of an electrocatalyst in proton ceramic fuel cells is very promising for CO_2 methanation[27] and pressurized H_2 production via steam

ADVANCED
SCIENCE NEWS

www.advancedsciencenews.com

NANO · MICRO

small

www.small-journal.com

electrolysis[28] or reforming of hydrogen carriers.[29] Therefore, high-pressure exsolution would be useful for pressure-needing technologies, but nowadays, the effect of pressure during the reduction treatment has never been considered to control or modify certain properties of the exsolved catalytic NPs.

In this work, we focused on the $Sr_2Fe_{1.5}Mo_{0.5}O_{6-\delta}$ double perovskite family to explore the effect of high-pressure exsolution. This kind of materials are widely studied due to their good properties as electrodes for energy conversion devices and solid-oxide electrochemical cells[30–38] and the possibility of, easily, introducing alternative atoms in B-sites. The partial substitution of Fe with other metallic atoms improves some of the material's properties[37,38] and even provides the direct exsolution of alloyed NPs.[6,39–43] For instance, FeCoNi ternary alloyed NPs were obtained via thermal exsolution of $Sr_2FeCo_{0.2}Ni_{0.2}Mn_{0.1}Mo_{0.5}O_{6-\delta}$, the material used in this work. In addition, changing the reduction temperature made it possible to tune the dispersion and size of these NPs and their composition.[44] Here, we demonstrate low-temperature exsolution when pressure is applied during the treatment. Also, proof of the possibility of deeply tuning NP composition with pressure changes is provided. In fact, after testing different treatment pressures (10, 50, and 100 bar), we stated that pressure enables the control of the alloy composition of the exsolved NPs, especially when compared to atmospheric pressure exsolution at the same temperature. In addition, these results also show, for the first time, that exsolved NPs can form and remain stable under pressure conditions, even as high as 100 bar in pure H_2.

2. Experimental Section

2.1. Material Synthesis

Single-phase powders of $Sr_2FeCo_{0.2}Ni_{0.2}Mn_{0.1}Mo_{0.5}O_{6-\delta}$ were synthesized by a modified Pechini sol-gel method, following the same procedure carried out in our previous work.[44] The final sintering step (1100 °C, 12 h in air) resulted in a solid powder ground in an agate mortar with a pestle and finally sieved under 200 μm. These powders were used to perform exsolutions at different temperatures (300 and 600 °C) and pressures (1, 10, 50, and 100 bar). Each treatment was performed under pure H_2 flow for 2 h in a horizontal tubular stainless-steel furnace. The heating ramp was conducted under a N_2 atmosphere.

2.2. Physicochemical Characterization

Crystal phases before and after exsolution treatments were analyzed via powder X-ray diffractometry (PXRD). For this, a PANalytical CubiX diffractometer (Cuα1,2 radiation) equipped with an X'Celerator detector in Bragg–Brentano geometry was used. Rietveld refinements with X'Pert Highscore Plus software (version 3.0.0).

For the study of the morphology, both metal oxide and exsolved metallic NPs, electron microscopies were carried out. High Resolution Field Emission Scanning Electron Microscopy (HRFE-SEM) with a Zeiss GeminiSEM 500. For Transmission Electron Microscopy (TEM), a JEM 2100F 200 kV field was employed. Also,

Energy Dispersive X-ray spectroscopy (EDXS) was performed to study compositions of exsolved NPs with EDXS X-Max 80 Oxford Instruments. Compositional percentages for every metal forming the alloyed exsolved NPs were average values, calculated via EDXS point ID analyses from several NPs in each exsolved sample. To analyze the exsolved NPs dispersion and mean sizes, HRFESEM and TEM micrographs were processed using ImageJ (1.52a) software.[45] Gatan DigitalMicrograph (2.31.734.0) software was employed to study crystallographic parameters from TEM micrographs, namely interplanar distances (d-spacings) using Digital Diffraction Patterns.

Due to the high difficulty in analyzing the small exsolved NPs at 300 °C, X-ray photoelectron spectroscopy (XPS) was used to study their composition. These analyses were performed with a SPECs spectrometer, using an Al-Kα monochromatic source and an MCD-9 detector. It was also employed to analyze the remaining materials.

3. Results

3.1. Effect of Pressure on the Host Perovskite Lattice

For these exsolution experiments, $Sr_2FeCo_{0.2}Ni_{0.2}Mn_{0.1}Mo_{0.5}O_{6-\delta}$ (named as DP, double perovskite, from now on) material w as employed. A single-phased cubic double perovskite was obtained, with no impurities present in the PXRD diffractogram (Figure S1, Supporting Information). Several reduction treatments were performed at 600 °C and 2 h, under pure H_2 flow, varying the absolute pressure in the reactor (1, 10, 50, and 100 bar). **Figure 2a** presents the diffraction patterns of the pristine and treated samples. The reduced samples show a lattice expansion, as manifested by the shift in the main diffraction peak (2θ between 32 and 33°) toward lower 2θ values. This is a sign of the effective material reduction due to the formation of oxygen vacancies and the higher ionic radii of the reduced metallic cations. The calculated cell volumes (Table S1a, Supporting Information) reveal that pressure affects the reduction of the oxide lattice, reaching the highest cell volume after treatment at 50 bar and exhibiting a volcano-like trend (Figure 5a). On the other hand, it is worth mentioning the formation of a separate phase after 10 and 50 bar treatments: Ruddlesden-Popper (RP) Sr_3FeMoO_7 phase can be appreciated, whose main peaks appear at 31.3 and 32.2° (the latter one overlapping with the main signal of the synthesized double perovskite). This tetragonal (*I4/mmm*) crystal structure was observed previously after reduction at 800 °C in 5% H_2/Ar at atmospheric pressure but not after treatment at 600 °C.[44] Even if, in the present work, pure H_2 is used as a chemical-reducing agent, no RP phase formation can be seen after the 1 bar treatment. This fact can be explained by the pressure increase (and not the higher concentration of H_2) in the treatment, which may facilitate the reduction of the material, allowing the RP phase formation at lower temperatures (600 °C). This is consistent with the larger lattice expansion after reducing treatments at 10 and 50 bar compared to atmospheric pressure. Interestingly, as shown in Table S1 (Supporting Information), the RP phase appearance is much more noticeable after reduction at 10 bar, surpassing the original double perovskite (62.4% RP phase). Surprisingly, after the 50-bar treatment, the RP phase appears at a much lower percentage (18.1%), and remarkably, no RP phase forms after the 100-bar
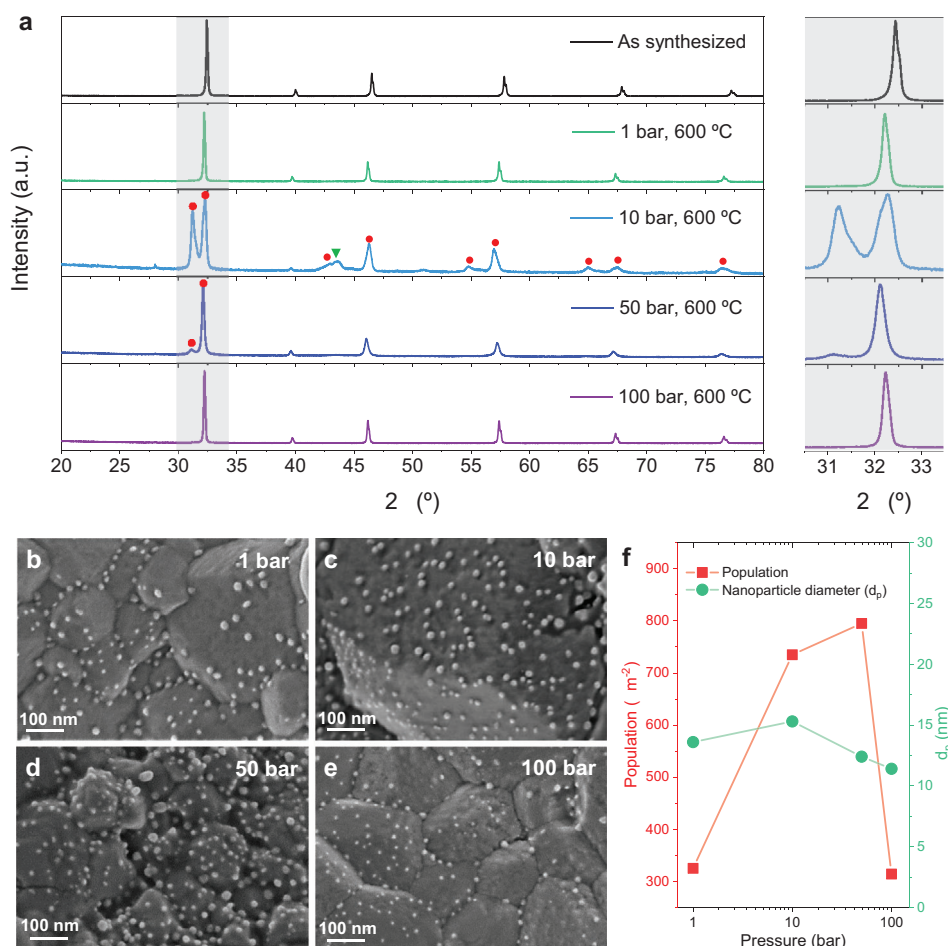
Figure 2. Powder X-ray diffraction patterns for $Sr_2FeCo_{0.2}Ni_{0.2}Mn_{0.1}Mo_{0.5}O_{6-\delta}$ before and after reduction treatments at 600 °C, 2 h under H_2 flow. Different treatment pressures were tested (1, 10, 50, and 100 bar). An additional phase is formed at 10 and 50 bar, and the Sr_3FeMoO_7 Ruddlesden-Popper phase shows up (red dots). a) Some metallic-phase signals can be appreciated after treatment at 10 bar (green triangles). HRFESEM micrographs of $Sr_2FeCo_{0.2}Ni_{0.2}Mn_{0.1}Mo_{0.5}O_{6-\delta}$ after exsolution treatments at 600 °C, 2 h under H_2 flow and different pressures: b) 1, c) 10, d) 50, and e) 100 bar. f) NPs size and populations change with different pressure treatments.

treatment. In addition, this highest-pressure treatment shows the slightest lattice expansion. It can be inferred from these results that increasing pressures enhance the reduction of the material until reaching a maximum at 50 bar and, at higher pressure, i.e., 100 bar, the perovskite reduction is limited, showing similar cell volumes as the one treated at atmospheric pressure. Furthermore, the enhanced material reduction is accompanied by the formation of the RP phase, namely, after treatment at 10 and 50 bar, while the RP phase is not detected after the treatment at 100 bar. In addition, some metallic-phase signals can be appreciated in the diffractogram of the material treated at 10 bar and 600 °C, overlapping with some peaks of the RP phase, and are a first indication of the exsolution of metallic NPs (see Figure 2a).

3.2. Effect of Pressure on Exsolved Particle Size and Population

HRFESEM analyses of the treated DP samples (Figure 2b–e) reveal the formation of exsolved spherical-shaped NPs along the surface regardless of the applied pressure. As shown in Figure 2f, remarkable differences in NP dispersion can be appreciated. The fact that the 10 and 50-bar treatments showed larger lattice expansion after reduction than the 1 and 100-bar has a direct consequence in the amount of exsolved NPs: higher populations are obtained with the 10 (735 µm^{-2}) and 50-bar (795 µm^{-2}) treatments. On the other hand, the samples treated at 1 and 100 bar showed lower and very similar NP populations (325 and 314 µm^{-2}), which are consistent with the previously analyzed lattice expansions. The increase in pressure is, thereby, triggering NP exsolution till reaching an optimal value at 50 bar (same as lattice expansion); after this, a remarkable drop occurs when reaching higher pressures (100 bar). Thus, exsolution dispersion follows a trend similar to that described for lattice expansions. Regarding exsolved NP mean sizes, a slight diameter growth happens when pressure increases from 1 bar (13.6 nm) to 10 bar (15.3 nm). After this point, increasing the pressure leads to smaller NPs: 12.4 and 11.4 nm for 50 and 100-bar treatments, respectively. Despite this, size changes with pressure are not as notable as
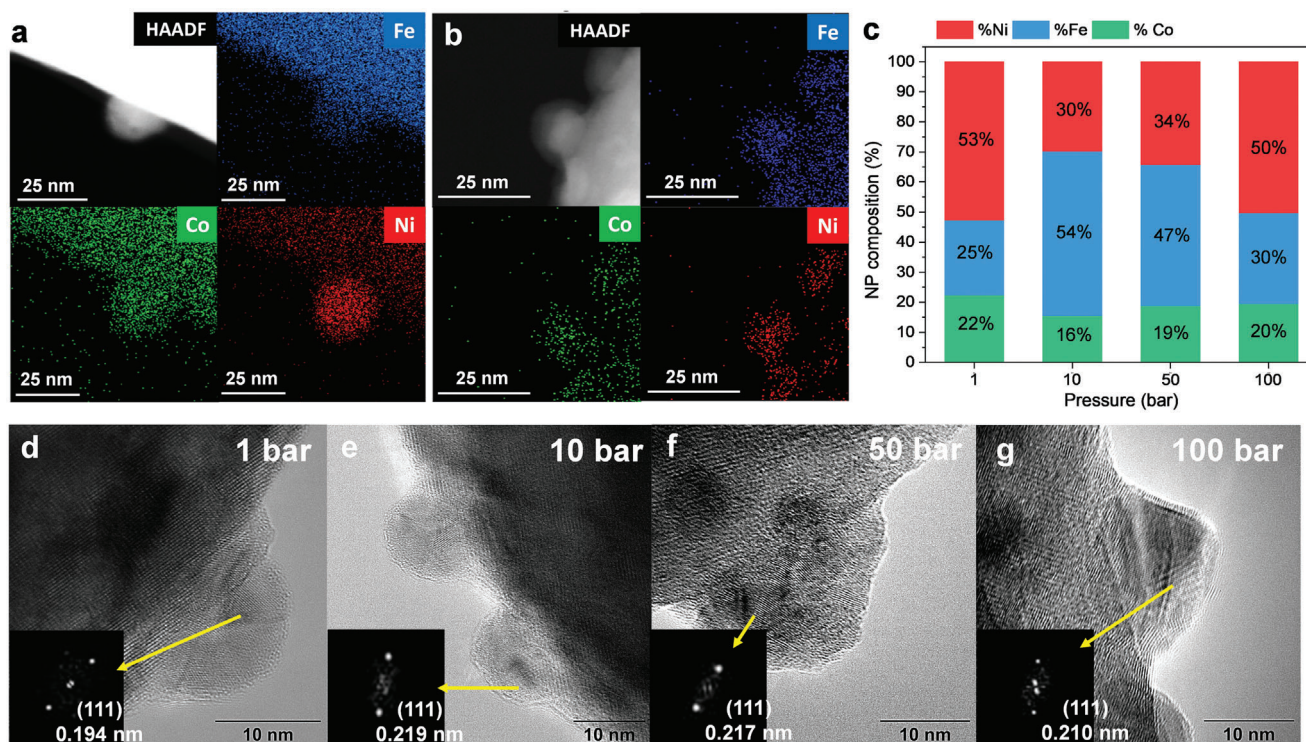
Figure 3. HAADF-STEM and map images of $Sr_2FeCo_{0.2}Ni_{0.2}Mn_{0.1}Mo_{0.5}O_{6-\delta}$ after 600 °C, 2 h exsolution treatments at a) 1 and b) 10 bar. Both treatments led to the exsolution of ternary alloyed FeCoNi NPs. c) Elemental composition of the exsolved NPs at different treatment pressures. HRTEM micrographs after exsolving 2 h at 600 °C for d) 1 bar, e) 10 bar, f) 50 bar, and g) 100 bar treatments and their corresponding digital diffraction patterns (DDP), showing interplanar distances corresponding to (111) planes.

surface population ones and remain almost constant. Histograms showing size distributions (Figure S2, Supporting Information) indicate that, as temperature and time, pressure can be a parameter to control morphological properties of the exsolved NPs (especially dispersion). A change in pressure (from 1 to 10 bar) greatly affects the population of exsolved NPs, namely, a two-fold increase. These tests also provided evidence, for the first time to our knowledge, that NPs can be exsolved under pressure, even as high as 100 bar, proving their stability beyond atmospheric pressure-reducing conditions. Finally, it is worth mentioning that some minor morphology changes can be appreciated, affecting the grain boundaries of the metal oxide after the 10 and 50-bar treatments. Those can be ascribed to the formation of the RP phase since it cannot be seen after treatment at 100 bar. This RP phase partial transformation is not expected to influence the morphological properties of the exsolved NPs since, upon reduction, the nucleation of exsolved NPs occurs before the RP phase appearance, and the NP growth is mainly associated with the increase in temperature.[44]

3.3. Effect of Pressure on Particle Composition

The NP composition was characterized to unravel the pressure impact during exsolution. Due to the remarkable differences between 1 and 10 bar exsolutions, a first comparison between them was performed. **Figure** 3a,b depict HAADF (High-angle annular dark-field)-STEM images and EDXS maps for 1 and 10-bar

treatments, respectively. In both cases, ternary alloyed FeCoNi NPs are obtained. No other elements can be appreciated forming these NPs, except some amount of O, indicating certain surface passivation (Figures S3 and S4, Supporting Information). Interestingly, there is a Ni depletion at the outer surface layers. This surface deficiency of exsolved atoms has already been studied by Wang et al. with Fe exsolution[46] and observed in our previous work with this particular material[44] for Ni and Co. This ternary alloy exsolution was also confirmed after treatment at 50 and 100 bar (Figures S5 and S6, Supporting Information, respectively). Elemental analyses of the NPs are shown in Figure 3c and, as expected, when exsolving at 1 bar, Ni is the main component of the exsolved NPs, representing almost 53% of the atomic fraction, followed by Fe (25%) and Co (22%). According to thermodynamic calculations,[47] Ni is the most reducible atom -and thus exsolvable- of the three studied cations here. Co and Fe show similar Gibbs free-energy values, which explains their almost equal presence in the exsolved NP. Knowing this, the compositional change observed after exsolving at 10 bar was remarkable since Fe becomes the main component of the alloyed NP (54%), showing a considerable growth in the atomic fraction. Ni content narrows (30%), and Co does not experience large changes (16%). This major presence of Fe remains after treatment at 50 bar (47%) but slightly decreases in favor of Ni (34%). After treatment at 100 bar, Ni is, again, the main atom forming the alloy (50 %), followed by Fe (30%) and Co (20%), being the composition of the exsolved NPs very similar to the 1 bar treatment ones. Thus, the two treatments exhibiting larger lattice expansion and exsolved NP

ADVANCED
SCIENCE NEWS
www.advancedsciencenews.com

NANO · MICRO
small
www.small-journal.com
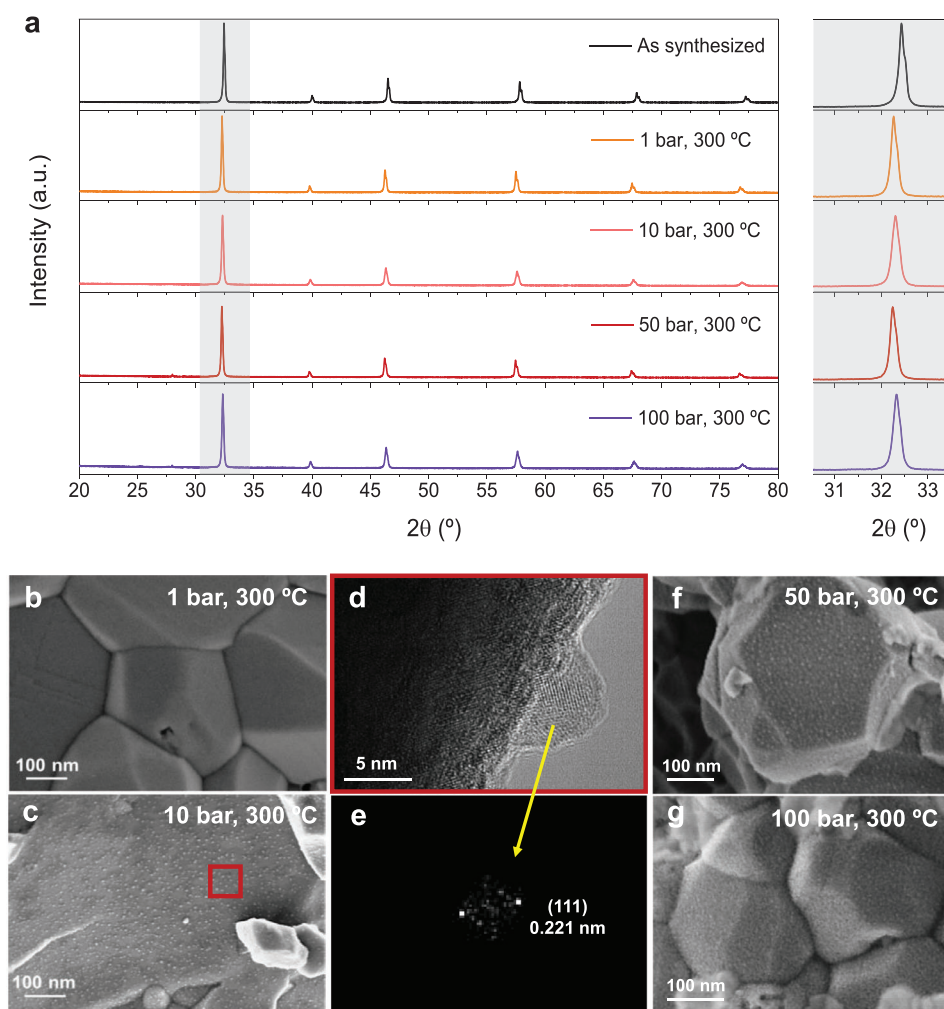
Figure 4. a) Powder diffraction patterns for $Sr_2FeCo_{0.2}Ni_{0.2}Mn_{0.1}Mo_{0.5}O_{6-\delta}$ before and after reduction treatments at 300 °C, 2 h under H_2 flow. Different treatment pressures were tested (1, 10, 50 and 100 bar). HRFESEM micrographs after reduction treatments at 300 °C, 2 h at b) 1 and c) 10 bar of pressure. No exsolved NPs can be seen at atmospheric pressure, but remarkable exsolution occurs by applying 10 bar. d) HRTEM micrograph of an NP after exsolving 2 h at 300 °C and 10 bar and e) the corresponding digital diffraction pattern (DDP). HRFESEM micrographs after reduction treatments at f) 300 °C, 2 h at 50, and g) 100 bar.
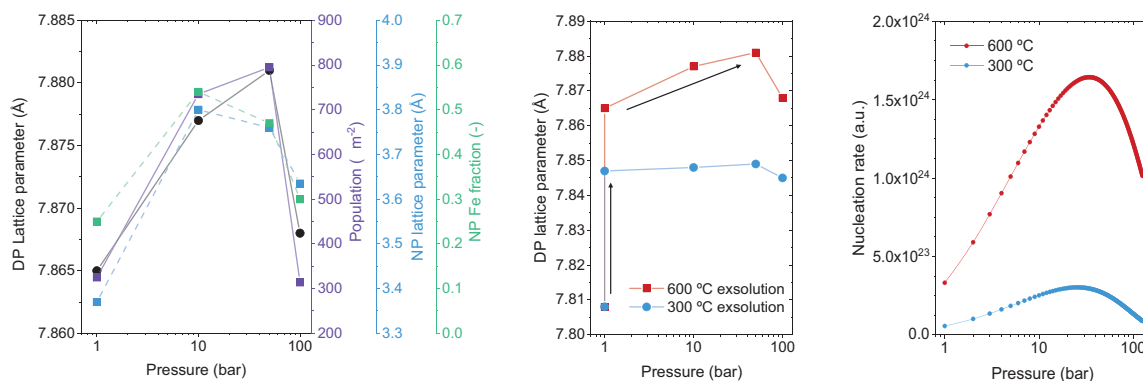
dispersion (10 and 50 bar) share the predominance of Fe in their exsolved NPs. Therefore, our results demonstrate a shifting in the equilibrium of Fe exsolution at certain pressures, inverting the expected compositional results for atmospheric pressure.

Figures 3d–g present high-resolution TEM images proving the anchored nature of the exsolved NPs after pressurized reduction treatments. The interplanar distances were measured using the corresponding Digital Diffraction Patterns (DDP), which exhibited a similar trend to that seen for atomic composition. After 1 and 100-bar treatments, the measured interplanar distances (0.194 and 0.210 nm, respectively) can be associated with the (111) planes of metallic phases (i.e., $FeNi_3$ = 0.207 nm). Nevertheless, after reduction at 10 and 50 bar, the d-spacings become larger than expected when compared to other metallic phases, both alloys and single metals, showing values of 0.219 and 0.217 nm, respectively. So then, NPs with higher content in Fe exhibit higher lattice parameters, as shown in Figure 5a.

The observed differences in the d-spacings between treatments can be related to the compositional variations of the exsolved alloys, but it cannot fully explain these crystallographic disparities. These effects will be discussed in the following sections of this work.

3.4. Lowering the Exsolution Temperature

To evaluate the influence of pressure over thermal exsolution requirements, reductions at 300 °C were carried out under the same conditions as for 600 °C treatments. A softer material's reduction is evidenced by the slighter lattice expansions (**Figure 4**; Table S1, Supporting Information) and the absence of RP phase formation. Slight differences in the lattice volume are observed among isothermal reduction treatments. Similarly to 600 °C exsolutions, a volcano-like trend can be appreciated when referring

**ADVANCED
SCIENCE NEWS**

www.advancedsciencenews.com

NANO · MICRO

small

www.small-journal.com

Figure 5. a) Variation of crystallographic parameters of the double perovskite and the exsolved NPs at different pressures for 600 °C treatments. b) Observed trend for DP lattice parameter when exsolving at 600 and 300 °C. c) Theoretical nucleation rate variation with pressure at the studied exsolution temperatures (300 and 600 °C).

to lattice expansions: the highest cell volumes are reached after treatment at 10 (483.4 Å^3) and 50 bar (483.5 Å^3), but increasing the pressure to 100 bar narrows the lattice expansion (**Figure 5**b). In addition, no impurities can be seen after any reduction, which confirms the stability of the material under pressurized conditions at 300 °C. Nevertheless, as shown in the following characterizations, some segregation of Sr occurs, forming amorphous oxides, which explains that no additional peaks appear in the PXRD analyses after reduction treatments. The Sr-surface segregation is ascribed to the exsolution process itself. B-site cationic deficiency after the generation of exsolved NPs occurs. Since the starting perovskite composition is A-site stoichiometric, SrO segregation happens, with the consequent charge balancing:

$$Sr_2FeNi_{0.2}Co_{0.2}Mn_{0.1}Mo_{0.5}O_{6-\delta} + \gamma H_2\,(g) \rightarrow$$

$$Sr_{2-\alpha}Fe_{1-x}Ni_{0.2-\gamma}Co_{0.2-z}Mn_{0.1}Mo_{0.5}O_{6-\delta-\alpha-\gamma} + \alpha SrO$$

$$+ Ni_\gamma Co_z Fe_x + \gamma H_2O\,(g) \qquad (1)$$
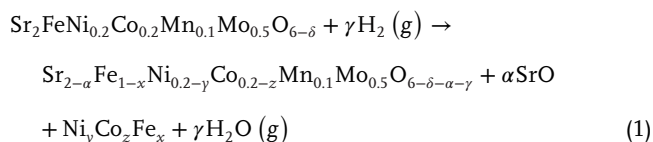
HRFESEM micrographs of the DP material after 1 and 10-bar exsolutions can be seen in Figure 4b,c. As expected, there is no exsolution after 1 bar reduction treatment. Nevertheless, by increasing the pressure to 10 bar, highly dispersed exsolved NPs emerge, with a mean size of 3.5 nm. In addition, other interesting facts can be analyzed here when compared to the exsolution at 600 °C and 10 bar. First, the size distribution of the exsolved NPs drastically narrows (histogram in Figure S7, Supporting Information). Second, as expected and depicted in Figure S8 (Supporting Information), notably smaller NPs (3.5 nm at 300 °C against 15.3 nm at 600 °C) are exsolved due to the lower temperature of the treatment (at higher temperatures, the growth rate of the NPs increases). Also, remarkably high surface populations are achieved, reaching 7072 μm^{-2}, almost ten times greater than at 600 °C (735 μm^{-2}). The NP population increase at lower temperatures was also predictable, as the nucleation rate increases when the exsolution temperature decreases. It is worth noting that

after 50 and 100-bar treatments, small NPs are spread all over the material in both cases, appearing almost as a textural change, especially in the case of 100-bar exsolution (Figure 4f,g).

HRTEM characterization was carried out to understand the properties of the exsolved NPs more deeply. Again, focusing on the 300 °C and 10 bar treatment (Figure 4d), a proper anchoring of the NPs is confirmed. Also, the interplanar distances from the exsolved NPs were measured using DDP (Figure 4e), and the (111) plane of the metallic phase, presenting a 0.221 nm d-spacing, could be identified. This value is close to the interplanar distance shown by NPs exsolved at 600 °C and 10 bar (0.219 nm), suggesting a similar crystallographic structure and composition of the NPs after exsolution at both temperatures. HRTEM characterization was also employed to confirm the emergence of small-sized, highly dispersed, spherical-shaped NPs after 50 and 100-bar reduction treatments (Figure S9, Supporting Information). These results show, for the first time, the possibility of functionalizing double perovskite materials with exsolved NPs at remarkably high pressures and low temperatures.

XPS analyses (Figure S10, Supporting Information) of Fe, Co, and Ni were performed to evaluate the possible formation of a ternary alloy in the NPs exsolved at 300 °C and 10 bar. Metallic Ni seems to be the main component of the exsolved alloys. Referring to Fe and Co, metallic phases can also be seen after the treatment but in lower amounts when compared to Ni. These results are consistent with the interplanar distances measured in these exsolved NPs, which suggested that the composition of exsolved NPs at 600 °C and 300 °C are similar when applying 10 bar.

In summary, the results in this section confirm the success of lowering the temperature requirements of thermal exsolution for this kind of double perovskites. When applying an increased pressure of 10 bar, highly dispersed, small, and homogeneously sized metallic NPs can be achieved at just 300 °C, being this temperature, to our knowledge, the lowest reported for thermal exsolution. This breakthrough improves thermal exsolution efficiency and enables in situ functionalization of materials at lower temperatures, expanding the range of processes where NPs exsolution can be leveraged.

**ADVANCED
SCIENCE NEWS**

www.advancedsciencenews.com

NANO · MICRO

small

www.small-journal.com

3.5. Discussing the Effects of Pressure During Thermal Exsolution

It is experimentally established that an increase in the treatment pressure has a remarkable impact on the morphological and compositional properties of the alloyed exsolved NPs. The morphological effects of pressure on NP exsolution -focusing on 600 °C treatments- are mainly related to their dispersion (Figure 2), seeing that size is not remarkably affected. The increase in NP exsolution extent after 10 and, especially, 50-bar treatments, compared to the atmospheric pressure, may stem from i) the higher ratio of reducing gas (H$_2$) collisions with the material's surface and ii) the compressive strain that pressure unleashes on the oxide. First, an increased H$_2$ pressure favors the exsolution process due to a kinetic effect, mainly due to a higher rate of oxygen-vacancy formation, which is preferential nucleation sites for metal NP growth (and so, exsolution),[18] according to:[19,48]

$$O_O^X = V_O^{\cdot\cdot} + 2e^- + \frac{1}{2}O_2 \qquad (2)$$

In addition, the increased H$_2$ pressure leads to higher reduction rates,[49] which should also be considered in the favored exsolution at higher pressures. This fact not only explains the larger lattice parameters seen when increasing pressure (except after 100 bar treatment, see Figure 5a) but also the formation of RP phase at 10 and 50 bar, which is not seen after atmospheric pressure treatment. Nevertheless, this statement could seem contradictory with the lower presence of the RP phase when increasing pressure treatment. At this point, competitive influence between two different pressure effects must be considered: favored chemical reduction and compressive strain due to the increased pressure. It is worth mentioning that, due to the mechanical properties of perovskite materials, which exhibit considerable Young modulus,[50,51] compressive strain effects shall be minor at these pressures when compared to chemical reduction. Nonetheless, increasing pressure, e.g., at 100 bar, would have non-neglectable effects regarding qualitative behavior concerning exsolution. Several works dealt with the influence of both tensile and compressive strain over exsolution in metal-oxide thin films. Han et al. observed an increased exsolution extent when applying compressive strain in La$_{0.2}$Sr$_{0.7}$Ti$_{0.9}$Ni$_{0.1}$O$_{3-\delta}$ (LSTN) thin films, showing a larger number of NPs and smaller particle sizes.[48] This may fit our observations in the slight drop in exsolved NPs size exhibited when increasing the treatment pressure from 10 to 50 to 100 bar (15.3, 12.4, and 11.4 nm, respectively). The higher mean sizes exhibited with 10-bar compared to 1-bar reduction (13.6 nm) may respond to the increased exsolution rate; a remarkably larger number of metallic atoms are exsolving, affecting mainly the dispersion but also the mean sizes. However, Wang et al. studies explained differences between enhanced exsolution with tensile and compressive strains. They observed increased exsolution rates in La$_{0.6}$Sr$_{0.4}$FeO$_{3-\delta}$ (LSF) with tensile strain but suggested an explanation for Han et al. results. To sum up, they expected enhanced exsolution with compressive strain if the oxide lattice compresses after exsolution treatment, and vice versa,[18] which fits with Han et al. results but not ours (double perovskite exhibits lattice expansion after exsolution at 1, 10, and 50 bar). We hypothesize that, until reaching a certain pressure, exsolution is
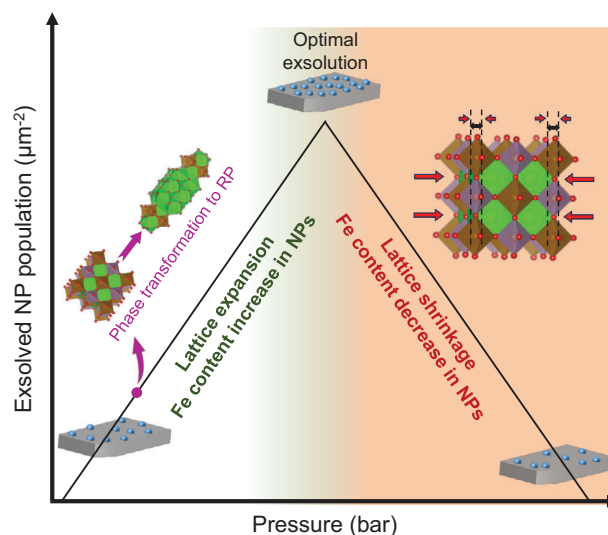
Figure 6. Schematic explanation of pressurized-reduction effects over exsolution and crystal phase impact on Sr$_2$FeCo$_{0.2}$Ni$_{0.2}$Mn$_{0.1}$Mo$_{0.5}$O$_{6-\delta}$. Volcano-plot-like influence of pressure is considered, based on the experimental results presented here, which indicate two main competing effects: enhanced chemical reduction due to higher H$_2$ collisions, thus more oxygen vacancies are created; and compressive strain. Due to visual reasons, the volcano-like plot is represented symmetrically. Nevertheless, our experimental results (see Figure 3e) show that the exsolution extent may reach an optimal value between 10 and 50 bar treatments, so the volcano-like trend would be asymmetric. A-site atoms (Sr) are represented in green; B-site atoms (Fe, Co, Ni, Mn) in brown; B-site Mo in purple; and O atoms in red in the crystal structures. Compressive strain is represented with red arrows, free space for cation diffusion reduction, with black arrows.

mainly controlled by chemical reduction, which is, in turn, kinetically enhanced by the increased pressure. Here, the increase in NP exsolution dispersion is due to two effects: i) the higher rate of reduction and oxygen-vacancy formation and ii) the compressive strain, which also influences the mean size drop and hinders the appearance of the RP phase (**Figure 6**). After reaching a certain pressure, exsolution rates start lowering, mean sizes keep dropping, and so does RP phase formation, meaning that compressive strain overcomes the kinetic effects of the higher H$_2$ collisions. Thereby, the lattice parameter (and cell volume) decreases beyond this point, hindering cation diffusion and, in turn, slowing down the exsolution process, thus directly affecting the dispersion of NPs (Figure 5a). To sustain exsolution, oxide ions and cations have to migrate to the surface. Transport of both species generally depends on free-space availability in the unit cell,[52] which hinders beyond certain pressure. This statement goes along with the lower lattice volume observed after 100-bar treatment compared to 10 and 50-bar exsolutions (see Table S1, Supporting Information) and the decrease in NP populations. Interestingly, the exsolved material at 600 °C and 100 bar shows (Figure S11, Supporting Information), at certain regions, some holes formerly occupied by exsolved NPs. A similar phenomenon was observed after acid-etching exsolved NPs [48] Thus, reaching certain pressure values may cause a loss of exsolved NPs.

These explanations are also compatible with 300 °C exsolutions (Figure 5b), where compressive strain at 100 bar even overcomes the predictable lattice expansion due to chemical

**ADVANCED
SCIENCE NEWS**

www.advancedsciencenews.com

NANO · MICRO

small

www.small-journal.com

reduction, and the lattice parameter is slightly lower than the one reached under atmospheric pressure. Regarding the exsolution results at 300 °C, pressure is key in triggering the nucleation process (Figure 4b,c). This fact can also be supported by the kinetic effect of increased pressure. It is worth noting that lowering the exsolution temperature increases the nucleation rate while increasing temperature favors NPs growth. So then, a lower exsolution temperature, together with the kinetic effect of increased collisions, shall explain the remarkable difference in NP populations when comparing 10-bar exsolution at 300 °C and 600 °C. In addition, the exsolved NPs seen after 50 and 100-bar exsolution are smaller than the ones exsolved at 10 bar, which also fits with the compressive strain effect over NP size explained for 600 °C exsolutions.

The classical nucleation theory[53–55] can also be considered to qualitatively explain the influence of applied pressure over nucleation rates, which can be expressed as:

$$J = A exp \left(\frac{-\Delta G^*}{kT} \right) \tag{3}$$

where J is the nucleation rate of NPs, A a pre-exponential factor, k the Boltzmann constant, T the temperature and ΔG^* the critical free energy for nucleation. This ΔG^* is given by:

$$\Delta G^* = \left(\frac{16\pi\gamma^3 V_m^2}{3\Delta G_v^2} \right) \tag{4}$$

Being γ the surface energy, V_m the molar volume of the nucleating phase and ΔG_v the driving force for exsolution. Referring to the latter, if it is, indeed, influenced by the applied pressure, and assuming ideal gas behavior, ΔG_v can be expressed as:

$$\Delta G_v (P) = \Delta G_v (P_0) - RT ln \left(\frac{P}{P_0} \right) \tag{5}$$

considering $\Delta G_v(P_0)$ the driving force at the reference pressure. In addition, the effect of pressure over γ shall also be considered and, according to Gibbs adsorption isotherm, the change of γ with pressure (P)

$$\left(\frac{\partial \gamma}{\delta P} \right)_T = -\Gamma \tag{6}$$

where Γ is the surface excess concentration of the adsorbed gas species (H_2). This negative Γ means a decrease in surface energy with increasing pressure. Combining both effects:

$$J(P) = A exp \left(\frac{-16\pi V_m^2 [\gamma (P)]^3}{\left[3kT \left(\Delta G_v (P_0) - RT ln \left(\frac{P}{P_0} \right) \right)^2 \right]} \right) \tag{7}$$

This suggests that J can be increased with applied pressure by reducing the surface energy and increasing the driving force for exsolution. For these calculations, several assumptions and typical values were considered (Appendix S1, Supporting Information). The calculated J variation with pressure can be observed in Figure 5c for both 300 and 600 °C. The theoretical trends are consistent with the experimental exsolution extent dependence with pressure observed at 600 °C and suggest a similar behavior for 300 °C. These theoretical calculations also suggest an optimal nucleation rate (volcano-like trend) for applied pressures between 10 and 50 bar, which correlates well with the experimental values. This model is valid if the surface energy has a small yet negative correlation coefficient with pressure (c parameter in Appendix S1, Supporting Information). It is worth mentioning that higher temperatures theoretically lead to higher nucleation rates, as seen in Figure 5c. However, this model only considers the energy for the nuclei formation process. So, this does not apply to the global exsolution phenomena since temperature increase also implies the growth of the formed NPs, leading lower exsolution temperatures to higher NP populations. Nevertheless, the theoretical model presented here is a good descriptor of the influence of pressure on the nucleation rate of the exsolved NPs, and it is coherent with the experimental observations assessed in this work.

Last, pressure also proved to have a remarkable impact on the composition of exsolved alloys. As expected at atmospheric pressure, Ni is the main component of the alloy, as it is the most favored metal to reduce, compared to Fe and Co.[47] The fact that Ni is more likely to exsolve has also been seen computationally.[56,57] Nevertheless, when applying 10 and 50-bar treatments, Fe becomes the main component of the alloy (see Figure 3c). As increasing pressure to specific values kinetically favors the material reduction (chemical reduction control), the reducibility of the three exsolvable cations may become more similar. Nevertheless, Fe represents a larger phase fraction in the metal oxide matrix, which explains that Fe is statistically more likely to exsolve under these conditions. At 100 bar, as exsolution is hindered by compressive strain, Ni becomes again the main component of the alloy. These compositional changes may also explain the observed differences in the d-spacings of (111) planes in the exsolved NPs since the interplanar distance trend is similar to the compositional rate: richer Fe NPs exhibit higher d-spacings. This observed trend may originate from electronic and nano-size morphologic effects. First, the lattice parameter (a) of Fe and Ni combined is higher than the single metals separately. This would explain the higher a values calculated when Fe content increases NPs exsolved at 10 and 50 bar (Figure 5a, Table S2, Supporting Information) and the unusually high d-spacings measured by HRTEM. Second, the higher a values may also be associated with abnormally stretched NPs. Due to the epitaxy relation between exsolved NPs and the metal oxide matrix, these NPs can be subjected to tensile strain from the matrix, as its lattice volume expands after reduction (see the similar trend in a values for exsolved NPs and the metal oxide matrix in Table S2, Supporting Information).

4. Conclusion

The effect of high pressure on ternary alloyed NP exsolution from $Sr_2FeCo_{0.2}Ni_{0.2}Mn_{0.1}Mo_{0.5}O_{6-\delta}$ was assessed here for the first time. Our results show that applying pressure has profound implications for the alloy composition. Namely, by increasing the pressures to 10 and 50 bar, Fe became the element with the highest concentration in the NPs, whereas, at atmospheric pressure, it is commonly Ni. Interestingly, by increasing the pressure to 100 bar, this trend was reverted again, Ni again being the element

with a higher presence in the FeCoNi alloyed NPs. Concurrently, it was observed that 10 and 50 bar total pressure led to the greatest extent of reduction at 600 °C, which, for the case of 10 bar, led to a crystallographic transformation toward a Ruddlesden–Popper phase. This implies that the maximum number of oxygen vacancies is obtained at 10 and 50 bar, thus leading to a higher NP exsolution extent. We also show that pressure can drastically lower the exsolution temperature to 300 °C, leading to a NP dispersion of one order of magnitude higher than at 600 °C. Overall, the results presented here demonstrate that pressure accelerates the kinetics of cation migration of elements commonly exsolved at a slower pace than Ni. However, this effect reaches its maximum at 10–50 bar, leading to a volcano-plot-like tendency, confirmed with theoretical calculations based on classical nucleation theory, of pressure and extent of exsolution, which might indicate that two competing mechanisms exist at higher pressures, e.g., 100 bar. These findings shed light on the effects of pressure in metallic NP exsolution, which might help in the design of exsolved alloys with adjustable composition, size, and dispersion, aiding in lowering exsolution requirements, with potential application in catalytic processes occurring at high pressures.

Supporting Information

Supporting Information is available from the Wiley Online Library or from the author.

Acknowledgements

Conflict of Interest

The authors declare no conflict of interest.

Data Availability Statement

The data that support the findings of this study are available from the corresponding author upon reasonable request.

Keywords

[1] D. Neagu, J. T. S. Irvine, J. Wang, B. Yildiz, A. K. Opitz, J. Fleig, Y. Wang, J. Liu, L. Shen, F. Ciucci, B. A. Rosen, Y. Xiao, K. Xie, G. Yang, Z. Shao, Y. Zhang, J. Reinke, T. A. Schmauss, S. A. Barnett, R. Maring, V. Kyriakou, U. Mushtaq, M. N. Tsampas, Y. Kim, R. O'Hayre, A. J. Carrillo, T. Ruh, L. Lindenthal, F. Schrenk, C. Rameshan, et al., *J. Phys. Energy* **2023**, *5*, 031501.

[2] K. Kousi, C. Tang, I. S. Metcalfe, D. Neagu, *Small* **2021**, *17*, 2006479.

[3] D. Neagu, T.-S. Oh, D. N. Miller, H. Ménard, S. M. Bukhari, S. R. Gamble, R. J. Gorte, J. M. Vohs, J. T. S. Irvine, *Nat. Commun.* **2015**, *6*, 8120.

[4] H. Chen, Y. Sun, S. Yang, H. Wang, W. Dmowski, T. Egami, S. Dai, *Chem. Commun.* **2020**, *56*, 15056.

[5] M. Santaya, C. E. Jiménez, H. E. Troiani, E. A. Carbonio, M. D. Arce, L. M. Toscani, R. Garcia-Diez, R. G. Wilks, A. Knop-Gericke, M. Bär, L. V. Mogni, *J. Mater. Chem. A* **2022**, *10*, 15554.

[6] H. Lv, H. Lin, X. Zhang, Y. Song, H. Matsumoto, C. Zeng, N. Ta, W. Liu, D. Gao, G. Wang, X. Bao, *Adv. Mater.* **2020**, *32*, 1906193.

[7] V. B. Vert, F. V. Melo, L. Navarrete, J. M. Serra, *Appl. Catal. B Environ.* **2012**, *115*, 346.

[8] Y. Nishihata, J. Mizuki, T. Akao, H. Tanaka, M. Uenishi, M. Kimura, T. Okamoto, N. Hamada, *Nature* **2002**, *33*, 8.

[9] D. Neagu, V. Kyriakou, I. L. Roiban, M. Aouine, C. Tang, A. Caravaca, K. Kousi, I. Schreur-Piet, I. S. Metcalfe, P. Vernoux, M. C. M. Van De Sanden, M. N. Tsampas, *ACS Nano* **2019**, *13*, 12996.

[10] V. Kyriakou, D. Neagu, G. Zafeiropoulos, R. K. Sharma, C. Tang, K. Kousi, I. S. Metcalfe, M. C. M. van de Sanden, M. N. Tsampas, *ACS Catal.* **2020**, *10*, 1278.

[11] S.-K. Otto, K. Kousi, D. Neagu, L. Bekris, J. Janek, I. S. Metcalfe, *ACS Appl. Energy Mater.* **2019**, *2*, 7288.

[12] J. Spring, E. Sediva, Z. D. Hood, J. C. Gonzalez-Rosillo, W. O'Leary, K. J. Kim, A. J. Carrillo, J. L. M. Rupp, *Small* **2020**, *16*, 2003224.

[13] Y. H. Kim, Y. Kang, S. Jo, H. Jeong, D. Neagu, J. Myung, *Chem. Eng. J.* **2022**, *441*, 136025.

[14] X. Sun, H. Chen, Y. Yin, M. T. Curnan, J. W. Han, Y. Chen, Z. Ma, *Small* **2021**, *17*, 2005383.

[15] N. Yu, G. Jiang, T. Liu, X. Chen, M. Miao, Y. Zhang, Y. Wang, *Sustain. Energy Fuels* **2021**, *5*, 401.

[16] J. Guo, R. Cai, E. Cali, G. E. Wilson, G. Kerherve, S. J. Haigh, S. J. Skinner, *Small* **2022**, *18*, 2107020.

[17] G. Chen, Y. Zhu, Y. Ying, Y. Yao, Z. Hu, D. Zu, Z. Lin, C.-W. Pao, Y.-C. Zhang, L. Li, Y. Zhu, H. Huang, *Matter* **2024**, *7*, 2265.

[18] J. Wang, J. Yang, A. K. Opitz, W. Bowman, R. Bliem, G. Dimitrakopoulos, A. Nenning, I. Waluyo, A. Hunt, J.-J. Gallet, B. Yildiz, *Chem. Mater.* **2021**, *33*, 5021.

[19] J. Myung, D. Neagu, D. N. Miller, J. T. S. Irvine, *Nature* **2016**, *537*, 528.

[20] V. Kyriakou, R. K. Sharma, D. Neagu, F. Peeters, O. De Luca, P. Rudolf, A. Pandiyan, W. Yu, S. W. Cha, S. Welzel, M. C. M. Sanden, M. N. Tsampas, *Small Methods* **2021**, *5*, 2100868.

[21] H. Khalid, A. ul Haq, B. Alessi, J. Wu, C. D. Savaniu, K. Kousi, I. S. Metcalfe, S. C. Parker, J. T. S. Irvine, P. Maguire, E. I. Papaioannou, D. Mariotti, *Adv. Energy Mater.* **2022**, *12*, 2201131.

[22] A. López-García, A. Domínguez-Saldaña, A. J. Carrillo, L. Navarrete, M. I. Valls, B. García-Baños, P. J. Plaza-Gonzalez, J. M. Catala-Civera, J. M. Serra, *ACS Nano* **2023**, *17*, 23955.

[23] J. Wang, K. B. Woller, A. Kumar, Z. Zhang, H. Zhou, I. Waluyo, A. Hunt, J. M. LeBeau, B. Yildiz, *Energy Environ. Sci.* **2023**, *16*, 5464.

[24] Y. H. Kim, Y. Jeong, B.-R. Won, H. Jeon, C. Park, D. Park, Y. Kim, S. Lee, J. Myung, *Nano-Micro Lett.* **2024**, *16*, 33.

[25] Q. Wang, J. Guo, P. Chen, *J. Energy Chem.* **2019**, *36*, 25.

[26] H. Liu, *Chin. J. Catal.* **2014**, *35*, 1619.

[27] I. Quina, L. Almar, D. Catalán-Martínez, A. M. Dayaghi, A. Martínez, T. Norby, S. Escolástico, J. M. Serra, *Chem Catal.* **2023**, *3*, 100766.

[28] E. Vøllestad, R. Strandbakke, M. Tarach, D. Catalán-Martínez, M.-L. Fontaine, D. Beeaff, D. R. Clark, J. M. Serra, T. Norby, *Nat. Mater.* **2019**, *18*, 752.

ADVANCED
SCIENCE NEWS

www.advancedsciencenews.com

NANO · MICRO

small

www.small-journal.com

[29] D. Clark, H. Malerød-Fjeld, M. Budd, I. Yuste-Tirados, D. Beeaff, S. Aamodt, K. Nguyen, L. Ansaloni, T. Peters, P. K. Vestre, D. K. Pappas, M. I. Valls, S. Remiro-Buenamañana, T. Norby, T. S. Bjørheim, J. M. Serra, C. Kjølseth, Science 2022, 376, 390.

[30] Q. Liu, X. Dong, G. Xiao, F. Zhao, F. Chen, Adv. Mater. 2010, 22, 5478.

[31] P. Qiu, S. Sun, J. Li, L. Jia, Sep. Purif. Technol. 2022, 298, 121581.

[32] Q. Liu, D. E. Bugaris, G. Xiao, M. Chmara, S. Ma, H.-C. zur Loye, M. D. Amiridis, F. Chen, J. Power Sources 2011, 196, 9148.

[33] Z. Xu, X. Hu, Y. Wan, S. Xue, S. Zhang, L. Zhang, B. Zhang, C. Xia, Electrochim. Acta 2020, 341, 136067.

[34] E. Santofimia, F. J. González, B. Rincón-Tomás, E. López-Pamo, E. Marino, J. Reyes, E. Bellido, Chemosphere 2022, 307, 135907.

[35] J. Meng, X. Liu, L. Han, Y. Bai, C. Yao, X. Deng, X. Niu, X. Wu, J. Meng, J. Power Sources 2014, 247, 845.

[36] J. Feng, G. Yang, N. Dai, Z. Wang, W. Sun, D. Rooney, J. Qiao, K. Sun, J. Mater. Chem. A 2014, 2, 17628.

[37] M. Gou, R. Ren, W. Sun, C. Xu, X. Meng, Z. Wang, J. Qiao, K. Sun, Ceram. Int. 2019, 45, 15696.

[38] Y. Jiang, Y. Yang, C. Xia, H. J. M. Bouwmeester, J. Mater. Chem. A 2019, 7, 22939.

[39] Y. Wang, T. Liu, M. Li, C. Xia, B. Zhou, F. Chen, J. Mater. Chem. A 2016, 4, 14163.

[40] Y. Yang, Y. Wang, Z. Yang, Z. Lei, C. Jin, Y. Liu, Y. Wang, S. Peng, J. Power Sources 2019, 438, 226989.

[41] H. Lv, L. Lin, X. Zhang, R. Li, Y. Song, H. Matsumoto, N. Ta, C. Zeng, Q. Fu, G. Wang, X. Bao, Nat. Commun. 2021, 12, 5665.

[42] H. Lv, L. Lin, X. Zhang, D. Gao, Y. Song, Y. Zhou, Q. Liu, G. Wang, X. Bao, J. Mater. Chem. A 2019, 7, 11967.

[43] X. Meng, Y. Wang, Y. Zhao, T. Zhang, N. Yu, X. Chen, M. Miao, T. Liu, Electrochim. Acta 2020, 348, 136351.

[44] A. López-García, L. Almar, S. Escolástico, A. B. Hungría, A. J. Carrillo, J. M. Serra, ACS Appl. Energy Mater. 2022, 5, 13269.

[45] C. A. Schneider, W. S. Rasband, K. W. Eliceiri, Nat. Methods 2012, 9, 671.

[46] J. Wang, A. Kumar, J. L. Wardini, Z. Zhang, H. Zhou, E. J. Crumlin, J. T. Sadowski, K. B. Woller, W. J. Bowman, J. M. LeBeau, B. Yildiz, Nano Lett. 2022, 22, 5401.

[47] A. J. Carrillo, K. J. Kim, Z. D. Hood, A. H. Bork, J. L. M. Rupp, ACS Appl. Energy Mater. 2020, 3, 4569.

[48] H. Han, J. Park, S. Y. Nam, K. J. Kim, G. M. Choi, S. S. P. Parkin, H. M. Jang, J. T. S. Irvine, Nat. Commun. 2019, 10, 1471.

[49] A. Habermann, F. Winter, H. Hofbauer, J. Zirngast, J. L. Schenk, ISIJ Int. 2000, 40, 935.

[50] N. Orlovskaya, M. Lugovy, S. Pathak, D. Steinmetz, J. Lloyd, L. Fegely, M. Radovic, E. A. Payzant, E. Lara-Curzio, L. F. Allard, J. Kuebler, J. Power Sources 2008, 182, 230.

[51] Y.-S. Chou, J. W. Stevenson, T. R. Armstrong, L. R. Pederson, J. Am. Ceram. Soc. 2000, 83, 1457.

[52] T. Mayeshiba, D. Morgan, Phys. Chem. Chem. Phys. 2015, 17, 2715.

[53] F. Liu, F. Sommer, C. Bos, E. J. Mittemeijer, Int. Mater. Rev. 2007, 52, 193.

[54] A. T. W. Kempen, F. Sommer, E. J. Mittemeijer, J. Mater. Sci. 2002, 37, 1321.

[55] V. Kalikmanov, Lecture Notes in Physics 860-Nucleation Theory, Springer International Publishing, Cham, Switzerland 2013.

[56] O. Kwon, S. Joo, S. Choi, S. Sengodan, G. Kim, J. Phys. Energy 2020, 2, 032001.

[57] J. H. Kim, J. K. Kim, J. Liu, A. Curcio, J.-S. Jang, I.-D. Kim, F. Ciucci, W. Jung, ACS Nano 2021, 15, 81.